Publications of the Astronomical Society of the Pacific
106: 890–908, 1994 August

The Goddard High Resolution Spectrograph: Instrument, Goals, and Science Results[1]

J. C. BRANDT[2]

Laboratory for Atmospheric and Space Physics, Campus Box 392, University of Colorado, Boulder, Colorado 80309-0392
Electronic mail: LYRAE::BRANDT

S. R. HEAP[2]

Laboratory for Astronomy and Solar Physics, Code 681, NASA/Goddard Space Flight Center, Greenbelt, Maryland 20771
Electronic mail: HRS::HRSHEAP

E. A. BEAVER[2]

Center for Astrophysics and Space Sciences, C-011, University of California, San Diego, La Jolla, California 92093-0111
Electronic mail: CASS05::BEAVER

A. BOGGESS[2]

Code 440, NASA/Goddard Space Flight Center, Greenbelt, Maryland 20771
Electronic mail: STSCI::BOGGESS

K. G. CARPENTER[2]

Laboratory for Astronomy and Solar Physics, Code 681, NASA/Goddard Space Flight Center, Greenbelt, Maryland 20771
Electronic mail: HRS::HRSCARPENTER

D. C. EBBETS[2]

Ball Aerospace Systems Group, P. O. Box 1062, AR1, Boulder, Colorado 80306
Electronic mail: LYRAE::EBBETS

J. B. HUTCHINGS[2]

Dominion Astrophysical Observatory, 5071 West Saanich Road, Victoria BC, Canada V8X 4M6
Electronic mail: hutchings@dao.nrc.ca

M. JURA[2]

Department of Astronomy, University of California, Los Angeles, California 90024
Electronic mail: BONNIE::JURA

D. S. LECKRONE[2]

Laboratory for Astronomy and Solar Physics, Code 681, NASA/Goddard Space Flight Center, Greenbelt, Maryland 20771
Electronic mail: HRS::HRSLECKRONE

J. L. LINSKY[2,3]

Joint Institute for Laboratory Astrophysics, University of Colorado and National Institute of Standards and Technology, Boulder, Colorado 80309-0440
Electronic mail: JILA::JLINSKY

S. P. MARAN[2]

Laboratory for Astronomy and Solar Physics, Code 681, NASA/Goddard Space Flight Center, Greenbelt, Maryland 20771
Electronic mail: HRS::HRSMARAN

B. D. SAVAGE[2]

Department of Astronomy, University of Wisconsin, 475 North Charter Street, Madison, Wisconsin 53706
Electronic mail: MADRAF::SAVAGE

A. M. SMITH[2]

Laboratory for Astronomy and Solar Physics, Code 681, NASA/Goddard Space Flight Center, Greenbelt, Maryland 20771
Electronic mail: HRS::HRSSMITH

L. M. TRAFTON[2]

MacDonald Observatory and Astronomy Department, University of Texas, Austin, Texas 78712
Electronic mail: lmt@astro.as.utexas.edu

F. M. WALTER[2]

State University of New York, Earth and Space Sciences, Stony Brook, New York 11794-2100
Electronic mail: fwalter@ccmail.sunysb.edu

R. J. WEYMANN[2]

Observatories of the Carnegie Institution of Washington, 813 Santa Barbara Street, Pasadena, California 91101
Electronic mail: rjw@ociw.edu

T. B. AKE[4]

Astronomy Program, Computer Sciences Corporation, Code 681, NASA/Goddard Space Flight Center, Greenbelt, Maryland 20771
Electronic mail: HRS::HRSAKE

F. BRUHWEILER[4]

Catholic University of America, Code 681, NASA/Goddard Space Flight Center, Greenbelt, Maryland 20771
Electronic mail: HRS::HRSFRED

J. A. CARDELLI[4]

Department of Astronomy, University of Wisconsin, 475 North Charter Street, Madison, Wisconsin 53706
Electronic mail: MADRAF::CARDELLI

D. J. LINDLER[4]

Advanced Computer Concepts, Code 681, NASA/Goddard Space Flight Center, Greenbelt, Maryland 20771
Electronic mail: HRS::HRSLINDLER

E. MALUMUTH[4]

Astronomy Program, Computer Sciences Corporation, Code 681, NASA/Goddard Space Flight Center, Greenbelt, Maryland 20771
Electronic mail: HRS::HRSELIOT

C. E. RANDALL[4]

Laboratory for Atmospheric and Space Physics, Campus Box 392, University of Colorado, Boulder, Colorado 80309-0392
Electronic mail: LYRAE::RANDALL

R. ROBINSON[4]

Astronomy Program, Computer Sciences Corporation, Code 681, NASA/Goddard Space Flight Center, Greenbelt, Maryland 20771
Electronic mail: HRS::HRSROBINSON

S. N. SHORE[4]

Department of Physics and Astronomy, Indiana University at South Bend, 1700 Mishawaka Avenue, South Bend, Indiana 46634
Electronic mail: HRS::HRSSHORE

G. WAHLGREN[4]

Astronomy Program, Computer Science Corporation, Code 681, NASA/Goddard Space Flight Center, Greenbelt, Maryland 20771
Electronic mail: HRS::HRSGLENN

Received 1993 October 6; accepted 1994 May 17

ABSTRACT. The Goddard High Resolution Spectrograph (GHRS), currently in Earth orbit on the *Hubble Space Telescope (HST)*, operates in the wavelength range 1150–3200 Å with spectral resolutions ($\lambda/\delta\lambda$) of approximately 2×10^3, 2×10^4, and 1×10^5. The instrument and its development from inception, its current status, the approach to operations, representative results in the major areas of the scientific goals, and prospects for the future are described.

1. INTRODUCTION AND METHODOLOGY

Planning for the instrument now called the Goddard High Resolution Spectrograph (GHRS) to be flown on the *Hubble Space Telescope (HST)* began more than 16 years ago. This paper summarizes major scientific objectives and the methodology that led to the instrument, the instrument itself, the in-orbit performance of the GHRS, fixes as a result of the servicing mission, and selected preservicing mission scientific results. As of this writing GHRS has passed all postser-

[1]Based on observations with the NASA/ESA *Hubble Space Telescope*, obtained at the Space Telescope Science Institute, which is operated by the Association of Universities for Research in Astronomy, Inc., under NASA contract NAS5-26555.

[2]GHRS Investigation Definition Team.
[3]Staff Member, Quantum Physics Division, National Institute of Standards and Technology.
[4]GHRS Science Team.

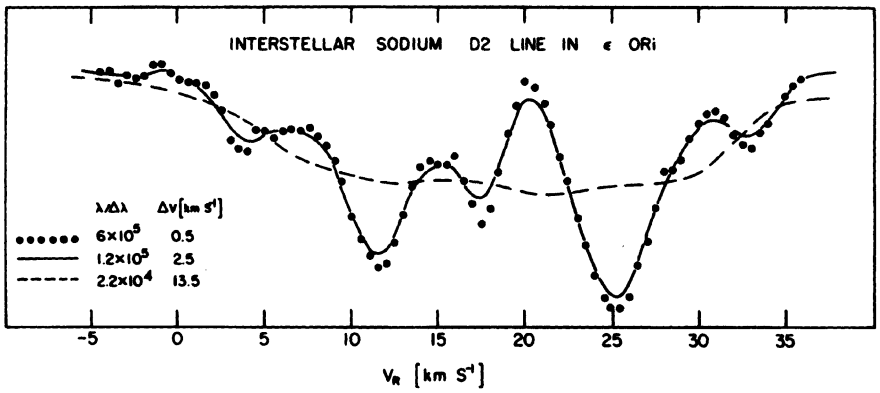

FIG. 1—Profile of a Na D_2 line at different resolving powers. The observations at resolving power of 6×10^5 are by Hobbs (1969) and most of the information is retained when smoothed to 1.2×10^5, but *not* when smoothed to 2.2×10^4. From the original proposal, "A High Resolution Spectrograph for the Space Telescope," July 1977; see Brandt (1991).

vicing mission orbital verification tests and is starting a new cycle of observations.

The process of creating a new space-science instrument should follow a logical path from the desired science to the needed measurements to the specific instrument. This process is not always followed and often a new instrumental technique "searches" for a problem to be solved. The GHRS Science Team felt that high-resolution spectroscopy in the ultraviolet could produce advances in many areas of scientific interest, and developed the instrument based on this premise.

The major scientific objectives of the GHRS Science Team were as follows (see Brandt 1991):

(1) *The interstellar medium*: Studies of the very local gas in the interstellar medium could yield (for example) a value for D/H. In dense clouds, molecule formation and the selective depletion of heavy elements could be investigated. From the spectra of distant stars, the composition and distribution of gas in adjacent spiral arms, the galactic halo, and the Magellanic clouds could be determined. Searches for as-yet undetected simple and very complex molecules in interstellar space could be carried out.

(2) *Mass loss by stellar winds and the evolution of the outer atmospheres of stars*: Studies of mass loss from OB supergiants in the Magellanic clouds and of coronal winds in late-type stars could be carried out. The mass loss, chromospheres, and circumstellar shells in red giants could be investigated. The mass transfer in binary stars, including X-ray binaries, could be studied.

(3) *Abundances of the elements and stellar evolution*: Abundances in stars with a wide range of ages could be measured to determine the chemical evolution of the galaxy.

(4) *Extragalactic sources*: Important studies of nearby quasars could be carried out and the physics of the nuclear regions of Seyfert galaxies investigated.

(5) *The Solar System*: Atmospheric structure in the major planets and their satellites could be determined. Auroral activity on the planets, particularly Jupiter, could be studied. The deuterium abundance in comets could be measured.

To date, we can report significant results obtained with the GHRS in all five areas of interest.

To carry out the science outlined above, we originally felt that the following capabilities or "design drivers" were needed: the spectrograph should have an ultraviolet response covering the wavelength range 1100–3200 Å and have spectral resolutions ($\lambda/\delta\lambda$) of $R=2\times10^4$ and 1.2×10^5. The instrument would need high sensitivity and high photometric precision. Because the proposed science mainly dealt with point sources, no angular resolution within the field of view was needed.

Note that some evolution occurred. We realized that a mode with spectral resolution of $R=2\times10^3$ covering the wavelength range 1100–1700 Å would be very useful and it was added. Also, we were not successful in obtaining a new echelle grating that would produce the mode with $R=1.2\times10^5$. A replica of an existing grating was used and $R\approx1.0\times10^5$ was achieved. We emphasize that a mode with $R\gtrsim1.0\times10^5$ was necessary to carry out some of our scien-

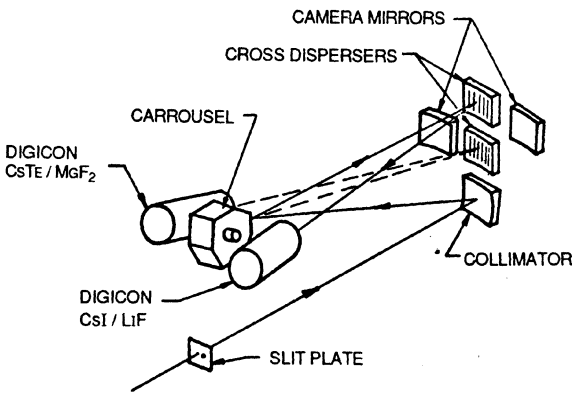

FIG. 2—Simple schematic of the GHRS.

tific objectives. Figure 1 shows the interstellar sodium D_2 line in Epsilon Orionis with $R=6\times10^5$ along with smoothed curves to simulate $R=1.2\times10^5$ and $R=2.2\times10^4$. Note that the curve with $R=1.2\times10^5$ contains most of the information in the original observations while the $R=2.2\times10^4$ curve does not come close.

The conceptual sketch of the GHRS is shown in Fig. 2. The spectrograph was developed by the Laboratory for Astronomy and Solar Physics, Goddard Space Flight Center. The prime contractor was Ball Aerospace Systems Group, Boulder, Colorado. The design philosophy stresses simplicity. The major moving part is the carousel which carries the gratings (except for the cross dispersers) and the acquisition mirrors. The other mechanism is the shutter which selects the aperture to be used, either the 0.25×0.25 arcsec aperture (small-science aperture or SSA), or the 2.0×2.0 arcsec aperture (large-science aperture or LSA) (also the fail-safe position). Two photon-counting 512-diode Digicons were chosen as the detectors. These have a dynamic range of 10^7 and are capable of 50-ms time resolution in rapid readout mode. Side 1 uses a CsI photocathode with a LiF faceplate to provide a higher sensitivity at the lower wavelengths and "solar blind" capability to wavelengths longer than about 1700 Å. Side 2 uses a $CsTe/MgF_2$ combination to cover the entire wavelength range of 1150–3200 Å. The wavelength limits are not rigid. In principle, the GHRS optics could be used down to about 1050 Å. The operating limit is ≈1150 Å. On the long-wavelength end, spectra have been obtained up to 3300 Å. The GHRS has four undispersed, UV-light target acquisition modes. Spectra can be obtained in seven spectroscopic modes: one first-order grating mode with $R\approx2000$ (1050–1700 Å only) designated G140L; four first-order grating modes with $R\approx20{,}000-35{,}000$ designated G140M, G160M, G200M, and G270M; and two echelle-grating modes with $R\approx90{,}000$ designated Ech-A and Ech-B.

The two sides of the instrument were intended to be largely independent and complementary, i.e., major parts of the science program could be carried out with either side. Progress reports during the construction of the instrument were given by Brandt et al. (1979, 1981, 1982, and 1984) and by Ebbets and Brandt (1983). The status after 1 yr in orbit was reported by Ebbets, Brandt, and Heap (1991).

2. THE GHRS STATUS AND PROSPECTS

2.1 The GHRS As Part of *HST*

The GHRS was designed to take advantage of the unique benefits of observing from orbit, and to provide instrumental capabilities which cannot be achieved at a ground-based observatory. These fall into four basic categories. First, and perhaps the most important, is access to the ultraviolet wavelengths which are absorbed by the Earth's atmosphere. The *HST* mirrors have aluminum surfaces with magnesium fluoride coatings. They allow the telescope to be useful for wavelengths from about 1150 Å in the vacuum ultraviolet to about 5 μm in the near infrared. The GHRS operates between 1150 and 3200 Å, providing access to the continua of hot sources, and important spectral lines for matter in the interstellar medium and stellar atmospheres.

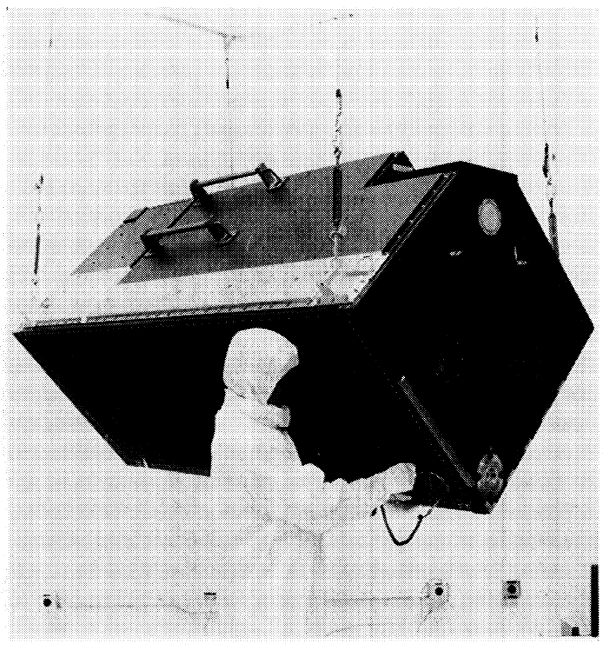

FIG. 3—The completed GHRS with the covers on. Note the handles for use by the astronauts. Courtesy of Ball Aerospace Systems Group.

Second, the dark skies in orbit present an extremely faint background in the ultraviolet. Care was taken with the optics and detectors of the GHRS to minimize backgrounds due to either stray light or electronic noise. In fact, the interactions of cosmic rays with the detectors appear to be the dominant background source for GHRS observations.

Third, the sharp images potentially obtainable above the blurring effects of the atmosphere motivate the use of very small entrance slits. The GHRS is capable of achieving a spatial resolution of 0.25 arcsec, making possible studies of stars in very crowded fields, and the detection of faint targets very close to brighter neighbors. This capability was degraded by the spherical aberration in *HST*'s primary mirror, but has been recovered after the installation of the Corrective Optics Space Telescope Axial Replacement (COSTAR) on the first servicing mission.

Finally, the absence of atmospheric variability and the capability for very stable pointing offer the prospects for high time resolution. The GHRS was designed to obtain time resolutions limited by instrumental capability to 50 ms at the short end, and limited only by scheduling constraints on the long end.

2.2 The Instrument

The GHRS is one of four axial bay science instruments (Fig. 3). It has two square entrance slits, located in the focal plane of the telescope 5.″34 arcmin from the optical axis. The LSA is 2.″00 arcsec on a side, and is used for target acquisition and for spectra of targets which are faint, or which do not require the maximum spectral resolution (full spectral resolution for point sources in the LSA was restored with the installation of COSTAR).

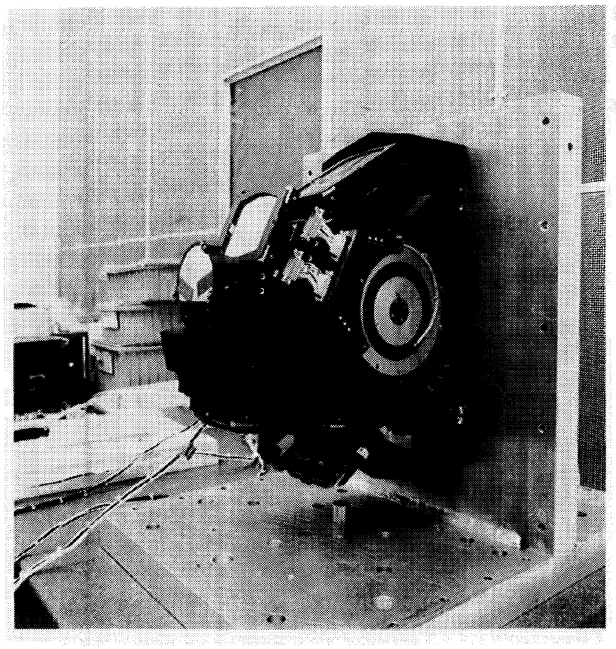

FIG. 4—The GHRS carousel with dummy optics, mounted on a test fixture. The GHRS echelle, first-order gratings, and target acquisition mirrors are mounted on the carousel and rotated into the correct position for observation. Courtesy of Ball Aerospace Systems Group.

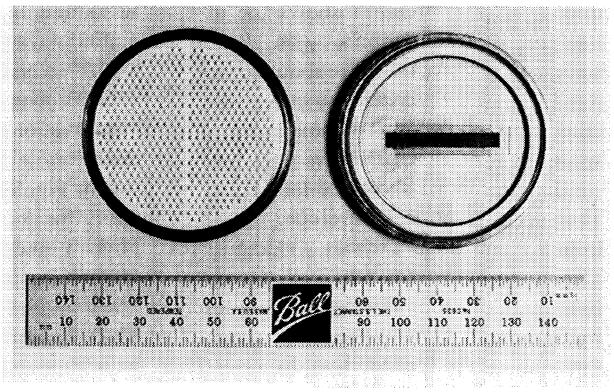

FIG. 5—The GHRS Digicon diode array and connector board; see Fig. 6. Each of the 512 diodes has its own wire going to the connectors, which lead to the preamplifiers. Courtesy of Ball Aerospace Systems Group.

The SSA is 0.″25 arcsec on a side, and is used when optimum spectral resolution, line profiles, and wavelength calibrations are critical. A collimator mirror directs the light to a carousel (Fig. 4), which holds one ruled and four holographic plane diffraction gratings used in first order, one echelle, and mirrors for four target acquisition modes. The desired optical element is engaged by rotating the carousel to place it in the collimated beam. Specific wavelengths can be selected by commanding the carousel to a particular position within the range available to each grating. The dispersed light is relayed to one of two camera mirrors for the first-order modes, or one of two concave cross-disperser gratings for the echelle. These elements focus the spectrum onto the photocathode of one of two Digicon detectors. Neither the focusing element nor the detector is selectable separately from the choice of grating. Individual photon events are detected in pulse counting mode, and accumulated in the memory of the *HST* onboard computer. The instrument contains Pt-Ne hollow cathode lamps to provide reference spectra for wavelength calibration, and Xe discharge lamps to flood illuminate the detectors for discriminator and deflection calibrations. A platinum spectrum measured to achieve full accuracy for wavelength determinations can be found in Reader et al. (1990).

2.3. The GHRS Detectors

The GHRS contains two 512-channel pulse counting Digicon detectors (Eck, Beaver, and Shannon 1985; Ebbets and Garner 1986); see Figs. 5 and 6. The two Digicons differ only in their faceplate material and photocathode composition. Detector "D1" has a semitransparent CsI photocathode deposited on a LiF window, covering the wavelength range from 1050 to 1800 Å; detector "D2" has a semitransparent CsTe photocathode on a MgF_2 window, covering the wavelength range from 1150 to 3200 Å. The GHRS detectors are controlled by the *HST* science computer, allowing most detector functions to be modified in order to perform scientific studies optimally.

The GHRS detector assembly, shown schematically in Fig. 6 and mounted on the optical bench in Fig. 7, consists of a Digicon tube, a permanent magnet focus assembly (PMFA) with trim focus coil and magnetic deflection coils, and a set of 512 charge-sensitive preamplifiers. In the Digicon tube, image photoelectrons are accelerated from the photocathode to the silicon diode target across a 22,500 V potential. The photoelectron image is focused onto the target by a 105 G field supplied by the PMFA. The field parameters are chosen such that the photoelectrons execute one gyro-loop in the time it takes to travel the 15 cm from the photocathode to the target array; photocathode to target image magnification is unity.

The GHRS Digicon target is composed of a linear array of 500 science diodes and twelve special purpose diodes, arranged as shown in Fig. 6; also see Fig. 5. Full impact of a 22.5 keV image photoelectron on a Digicon silicon diode causes the near instantaneous formation of a 5600 electron-hole pulse, well above the average 380 electron (RMS) electronic readout noise. The diode photoelectron pulses are counted by the independent diode channel amplifier, ratelimiter, discriminator, and counter electronics, allowing parallel readout of all 512 channels. Digicon target readout into the buffer counter memory occurs as photon events arrive to within the 7.8-μs time constant set by the rate limiter; readout noise is a relatively insignificant 10^{-5} false counts per second per diode channel. To develop a spectral image, a repetitive pattern of deflection steps is performed. Since the photoelectron guiding center motion is along the magnetic-field lines; the field caused by programmed current in the deflection coils shifts the image by an amount proportional to the magnetic-field shifts. The photon events from the array are accumulated in buffer memory for a frame time at the particular deflection step and then shifted and coadded into

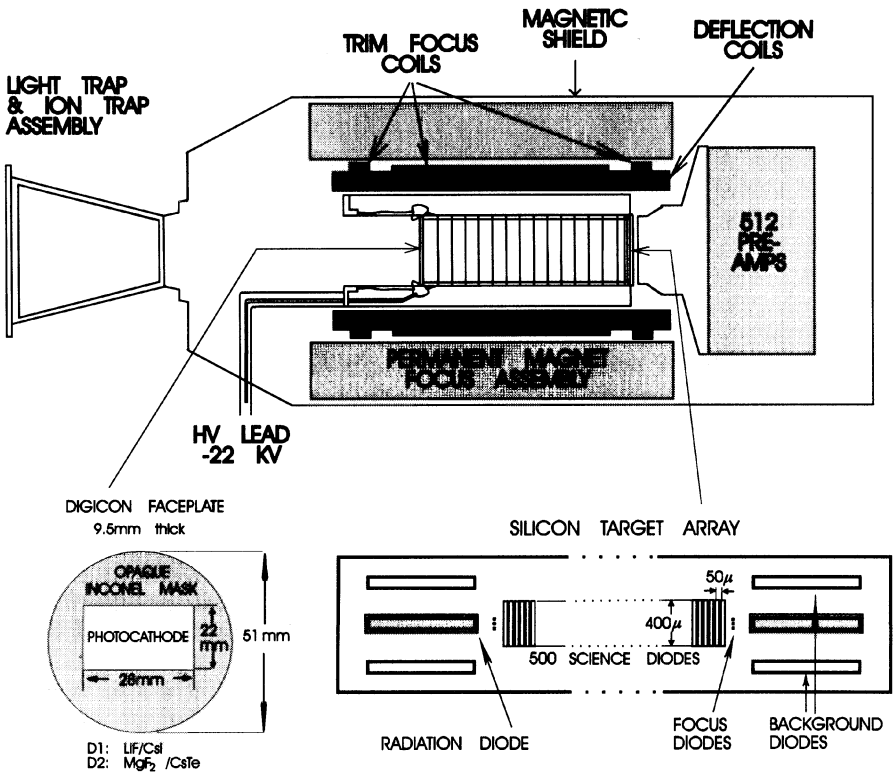

FIG. 6—Schematic of the GHRS Digicon detector assembly.

the appropriate array elements of the image array in the *HST* science computer. The frame time is user-specified down to a minimum of a 200-ms setting, the current default value. The primary deflection pattern is a series of consecutive deflection steps of $\frac{1}{4}$ diode pitch (12.5 μm) each along the diode array axis. This pattern is then repeated until completion of the science exposure. The 12.5 μm format is performed to fully sample the Digicon point spread function of about 40 μm FWHM to avoid data aliasing problems.

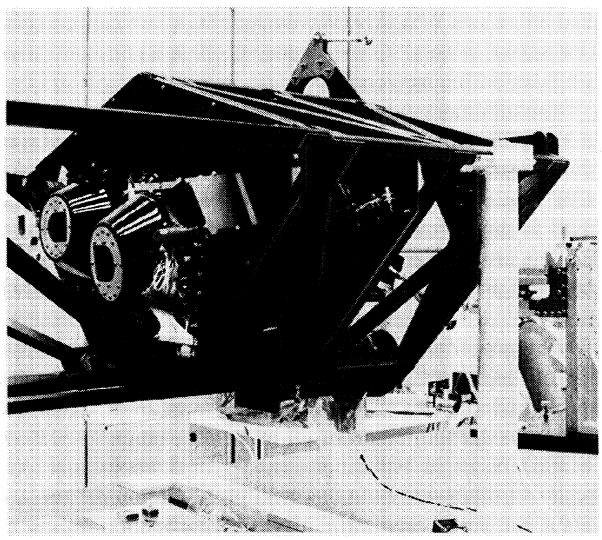

FIG. 7—GHRS detector assemblies mounted on the optical bench. Courtesy of Ball Aerospace Systems Group.

In-orbit GHRS D1 detector resolution is essentially unchanged from ground-test values. However, careful study of aperture and spectral line positions with time indicates a slightly larger than expected geomagnetically induced image motion problem (GIMP) in the D2 detector. The D2 mu-metal magnetic shield (shown in Figs. 6 and 7) inadequately attenuates the Earth's B field. The character of the image motion is a sinusoidal-like function with a frequency of two cycles per 96-min orbit and worst-case peak-to-peak amplitude of about one half of a diode.

The GIMP effect has been studied in detail (Baity et al. 1993) and a technique has been developed to remove this subdiode size image movement, if required. Since GHRS science data can be read out every few minutes, each differential readout is recentered during ground reduction processing according to the computed shift determined by the geomagnetic image motion model. The Earth's magnetic field is accurately modeled and fairly stable for the *HST* near-Earth orbital region (Wertz 1978). A computer program calculates the Earth's B field in the GHRS detector reference frame for each readout orbital position. The image shift in the GHRS Digicons is measured to be primarily correlated with the Earth's B-field vector. The scale factor for D2 is 40 μm per

Gauss of Earth's B field. Uncorrected, the worst-case peak-to-peak variation of about 0.5 G of the Earth's B field in the GHRS reference frame would cause a 20-μm image shift in the D2 detector, whereas corrected, this worst-case D2 GIMP is reduced by at least a factor of 4 to about 5 μm.

During the extensive ground-test activity, the GHRS detectors registered noise levels at high voltage of about 4×10^{-4} cts diode^{-1} s^{-1} (cds). In the near-Earth orbit of the *HST*, the radiation environment elevates the background to about the GHRS background specification of 0.01 cds. Modeling of the GHRS orbital background indicates that the predominant source of orbital noise comes from Cerenkov light generated by cosmic rays passing through the Digicon faceplate (Beaver et al. 1992). It is calculated that on average, a single cosmic ray passing through the faceplate results in the instantaneous burst of several thousand photons onto the Digicon photocathode. However, due to geometric dilution and other attenuation losses, only about 14% of the cosmic rays incident on the faceplate cause diode count events, at an average of about three counts per diode array per event (Rosenblatt et al. 1991).

To suppress burst noise, the GHRS design includes high-speed anticoincidence electronics. This circuit analog sums the output of all 500 science diodes within a 4-μs time constant. If the analog sum is greater than a preset limit, then the burst data can be rejected depending on the state of the anticoincidence flag. Tests indicate that this preset limit cannot be usefully set lower than eight counts. A limit setting below this level leads to excessive frame rejection caused by electronic noise solely related to the anticoincidence summing circuit. However, a preset limit count of eight reduces the GHRS detector background by about 15%. For burst rejection below an eight count limit setting, another GHRS observing option called on-the-fly-adder rejection (OTFA rejection) is available. Implementation of this software algorithm causes each 500 diode buffer frame to be summed and compared to a preset limit count. The diode count buffer is added into the GHRS image array in the *HST* science computer only if the OTFA (the sum) is less than the rejection limit value. Tests indicate that the OTFA-rejection algorithm reduces the GHRS detector background by a factor of 5 to about 0.002 cds for the rejection limit setting of two counts. Although OTFA rejection should improve GHRS limiting magnitude performance, the limit test value must be chosen with extreme care to avoid discarding too many object counts.

2.4 Operational Approach

The GHRS operates in an almost totally preplanned and autonomous mode. There is little real-time control except for an occasional intervention with a difficult target acquisition. The observer uses the standard proposal process to specify all of the parameters needed to define an observation, including grating, wavelengths, exposure times, scanning strategies, and calibration requirements. These are translated by the Space Telescope Science Institute (STScI) into commands which become part of a weekly Science Mission Specification. The GHRS observations begin execution at predetermined times during the week. Tables of parameters are used by the flight software to configure the instrument, acquire the target, accumulate the spectral data, monitor the safety of the spectrograph, and communicate with the spacecraft. An observation generally contains a target acquisition sequence, and one or more spectral exposures. Fully autonomous on-board acquisitions are the most common, although interactive acquisitions are available for complex targets. The software will drive the telescope through a search pattern, and recognize the target either as the brightest object in a 10×10 arcsec field, or as the first object encountered whose flux falls within a specified range. Locate and peakup algorithms center the target in either of the two apertures with a precision of approximately 30 milliarcsec for stars. As an option, the observer may specify that an image of the field in the aperture be made to verify the acquisition.

Spectra may be taken either in an accumulation mode or in a rapid readout mode. Accumulation mode offers a wide range of options for flight software control of exposure. The spectrum may be substepped on the diode array to oversample the resolution element, comb-added to reduce the effect of a few anomalous channels, and split into subexposures to separate the spectrum from detector fixed pattern noise.

The scattered light background may be sampled with the full diode array, and real-time rejection of cosmic-ray noise events may be enabled. To minimize risk of noise events or thermal or magnetic effects in the data a long exposure may be divided into a number of shorter integrations (typically 5 min each), which can be repeated with little penalty in overhead time. The one-dimensional detectors record only a limited range of wavelengths in a single exposure, ranging from about 6 Å with the echelle used at the shorter wavelengths to about 285 Å with G140L. Many observing programs require more data than can be had in a single exposure, and multiple settings are required. In most cases the desired central wavelengths are simply listed as individual exposures. If a long continuous region is preferred, the sequence may be specified either as a WSCAN (Wavelength SCAN along one spectral order), or an OSCAN (Order SCAN at a constant carousel position for the echelle.)

The minimum exposure time for ACCUM mode observations is 0.8 s, but the minimum time between exposures (i.e., the fastest time resolution) is approximately 30 s. If greater time resolution is desired, the RAPID readout mode may be used to sample the spectrum at intervals of 0.05–12.75 s, in increments of 0.05 s. None of the exposure control features of the flight software are available during a RAPID observation.

One novel feature of the GHRS data-acquisition process is real-time compensation for the Doppler shift introduced by the orbital velocity of the *HST*. For a target near the orbital plane, wavelength shifts of up to 18 data points (4.6 diode widths) occur in the echelle modes, and up to four data points (1 diode width) in the medium-resolution modes. The flight software keeps track of the orbital motion during an ACCUM mode exposure, and adjusts the "x component" (parallel to the direction of dispersion) of the detector magnetic deflection system once per minute to minimize the

spectral smearing that would otherwise occur. This adjustment causes a fixed wavelength in the spectrum to be coadded into the same data point despite its optical image moving in a predictable manner on the photocathode.

The data are stored on an on-board tape recorder at the conclusion of the exposure. They are relayed to the ground at preplanned times, and are sent to the Space Telescope Science Institute. There the raw data are processed, reduced with standard calibration procedures, archived, and delivered to the observer. Data tapes are usually available to the observer within 2 days after the observations take place.

2.5 In-orbit Status

The GHRS has been operating in orbit for more than 3 yr. Activities in the first several months after launch were devoted to Orbital Verification (OV) of the engineering and functional performance. This was followed by a Science Verification (SV) program, which established the initial instrument calibration, and demonstrated the core modes of operation (Ebbets 1992). Ongoing calibration activities by the STScI provide refinements and maintenance of the database, and the development of new capabilities.

The geometrical and sensitivity factors required for target acquisition were established during OV and SV, and recently have been extended to enable the "return to brightest point" option, and to improve the centering of targets in the SSA. Several UV standard stars have been observed to establish the sensitivity functions of all grating modes, and to characterize the "ripple function" of the echelle. These data also allowed subtle effects such as vignetting, detector blemishes, and photocathode granularity to be quantified. Measurements of the depths of saturated interstellar absorption lines were used to calibrate the algorithm used to remove scattered light from the raw data (Cardelli et al. 1989; 1993a). A large database of observations of the on-board lamps has facilitated a very sophisticated model for the wavelength calibration, which now includes adjustments for the carousel position, irregularly spaced subexposures, aperture offsets, thermal drifts, and a slight sensitivity to the projected component of the geomagnetic field on the detectors. Observations of sharp lined stars, and calculations made with the STScI Telescope Imaging Model software, have verified the spectral resolving power of the GHRS, and demonstrated the utility of several deconvolution techniques.

In general the performance is consistent with the design of the GHRS, and with the results of the ground-based test programs. The wavelength range, sensitivity, and resolving power all appear to be nominal. In particular, the sensitivity of the GHRS does not show any significant decline. The background count rates in the detectors are gratifyingly low. The recommended strategy of breaking long exposures into a series of 5-min subexposures minimizes the small smearing that might be caused by thermal or magnetic effects. The precise wavelength scales assigned by the calibration software allow the spectra to be combined with no loss of resolution. When the subexposures are made at slightly different grating positions, as with the standard FP-SPLIT procedure, they can be combined so as to eliminate the granularity of the detector photocathodes from the signal. We recommend that all observations, if possible, use the FP-SPLIT=4 option. The signal-to-noise ratio of the net spectrum is then found to scale as the square root of the total number of counts per pixel, as expected from counting statistics alone. In practice we have achieved S/N>400, with no indication that this is limited by anything other than photon noise.

The spherical aberration in *HST*'s primary mirror had several effects on the performance of the GHRS prior to the first servicing mission. Some details of the flight software were modified to adapt the target acquisition procedures to the unusual image shapes. These were successful, and led to robust acquisitions during the first three and a half years of observations. The SSA had been designed to intercept the core of the nominal *HST* image. The aberration caused a significant loss of throughput (down to about 20% of prelaunch estimates), and necessitated longer exposure times. On the other hand, the spectral resolving power remained unaffected for targets observed with the SSA, and the full GHRS performance was preserved. The LSA is large enough to accept most of the light, and its throughput is nominal. The line spread function for the LSA had a sharp core, but elevated wings, which resulted in diminished resolution (by about a factor of 2) and peculiar line profiles. The aberration also degraded the spatial resolution, and with it the ability to record the spectra of individual targets in crowded fields. Finally, the ability to observe faint sources was affected. For extended sources, the resolution and sensitivity remained unchanged, although the area sampled is larger. Basically, most scientific programs were still carried out with the GHRS and most of the losses were recovered by the successful COSTAR installation. A detailed discussion of GHRS in-orbit performance—sensitivity, spectral resolution, dark noise, etc.—will be given in the follow-on paper by Heap et al. (1994).

The GHRS experienced two hardware anomalies in its first three years. A problem in one set of carousel drive electronics caused some undependable behavior, but was resolved by reprogramming the operations to use a cross-strapped control mode. An intermittent electrical connection in a side 1 low-voltage power supply necessitated suspending use of the D1 detector until a repair was made during the first servicing mission. The problem precluded the use of gratings G140L and G140M and Ech-A until after the repair was made. The weakened power supply was used to transfer data from both detectors from the instrument to the spacecraft computers. It worked reliably with side 2 data transfer as its only load, apparently as long as it did not get too cold. During the first service mission a redundancy kit was installed to provide an alternate data path for the D2 detector, secure from possible further degradation of the side 1 power supply.

3. SCIENTIFIC RESULTS

In this section, we briefly describe examples of scientific results already available. The organization will be the same as the items in the major scientific objectives given in the Introduction and Methodology section above.

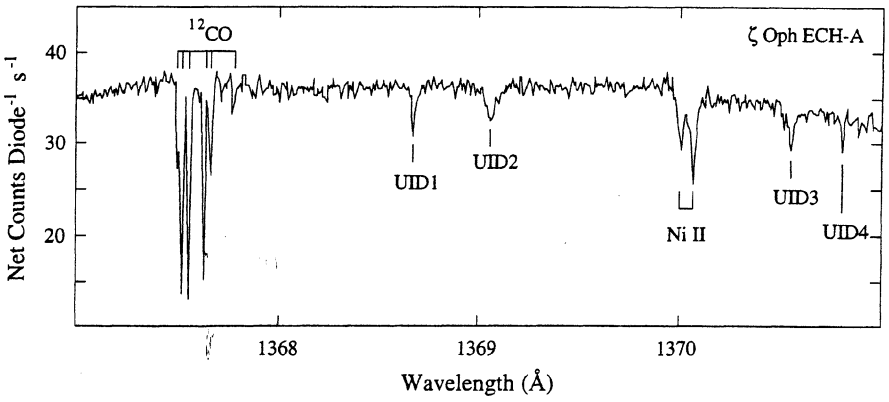

FIG. 8—An example of an echelle-A spectrum of ζ Oph centered at about 1369 Å. The data correspond to a continuum signal-to-noise of about 70. The lines marked "UID" are unidentified.

3.1 The Interstellar Medium

3.1.1 ξ Persei and ζ Ophiuchi

GHRS echelle observations of these two stars have produced very accurate interstellar atomic abundances for a large number of elements (Cardelli et al. 1991a; Savage et al. 1991; Cardelli, Savage, and Ebbets 1991; Savage, Cardelli, and Sofia 1992) and have provided important information on molecular CO and cloud physical conditions (Smith et al. 1991; Sheffer et al. 1992).

An example of an echelle spectrum of zeta Ophiuchi, centered at 1369 Å, is shown in Fig. 8. The benefits afforded by high resolution are clearly apparent in the ^{12}CO profile for which the individual rotational lines have been clearly resolved. Analogous observations of ^{13}CO have resulted in definitive evidence for CO fractionation toward ζ Oph (Sheffer et al. 1992). In addition, the Ni II profile clearly shows two principal cloud components at $V_{\rm lsr}=-27$ and -15 km s^{-1}. Detailed analysis of these two components for Ni II as well as for other elements has lead to new information regarding the interaction between gas and dust (Savage, Cardelli, and Sofia 1992). Finally, the spectrum shows several very weak features for which no positive identification exists. However, Tripp, Cardelli, and Savage (1994) have concluded that the broad feature labeled UID2 is probably a diffuse interstellar band which, if true, makes it the first of its kind ever found in the vacuum ultraviolet.

As indicated in Fig. 8, one of the most significant attributes of the GHRS is the ability to produce unprecedented UV data on weak absorption lines (e.g., with equivalent widths of $W(\lambda)<1-2$ mÅ). This capability comes largely through the ability of the GHRS to produce very high signal-to-noise photon-limited data (e.g., S/N$\gg$100).

For example, the GHRS has been used to obtain data on important abundant species like carbon through the weak intersystem C II line at $\lambda=2325$ Å toward Xi Persei [$W(\lambda)=1.42\pm0.41$ mÅ, S/N=160; Cardelli et al. 1991] and ζ Oph [$W(\lambda)=0.52\pm0.12$ mÅ, S/N=450; Cardelli et al. 1993a]. Analysis of weak lines also provides the opportunity to explore moderate to strong transitions of elements with relatively low cosmic abundances (i.e., less than 1 atom per 10^8–10^9 H atoms). GHRS observations of ζ Oph have produced new results for low abundance species including B II and Co II (Federman et al. 1993) and the first measures of the heavier-than-Zn ($Z>30$) elements Ga II, Ge II, As II, Kr I, and Sn II (Cardelli, Savage, and Ebbets 1991; Cardelli et al. 1993c). [We note that the Sn II measurement of Cardelli et al. (1991) was listed as an unidentified line; credit for the first identification of this transition as Sn II goes to Hobbs et al. 1993.] What makes these heavy elements important is that they arise from nucleosynthetic pathways (*s* and *r* process) uniquely different from those that produce Zn and the lighter elements and thus offer the opportunity to study the effects of nucleosynthetic enrichment and mixing of the interstellar gas.

A summary of the atomic abundances, normalized to meteoritic abundances (Anders and Grevesse, 1989) and plotted against condensation temperature (Wasson, 1985), is shown in Fig. 9 for the $V_{\rm lsr}=-15$ km s^{-1} component toward ζ Oph. As seen in the figure, most elements show some degree of underabundance relative to solar, with this underabundance increasing as the elemental condensation temperature increases. The standard explanation for this underabundance is that these elements have been removed from the gas phase because of their incorporation into interstellar dust grains. Most notable among these elements is Kr I which shows an abundance that is a factor 2 (-0.3 dex) below solar. However, because Kr I is a noble gas with a small van der Waals force, we find it unlikely that this underabundance is the result of Kr being incorporated into dust. The most likely explanation is that there is an error in the adopted reference solar abundance. Therefore, the measured abundance of Kr is most likely the true "cosmic" abundance, at least toward ζ Oph.

3.1.2 D/H in the Line of Sight Toward Capella

Just as a picture may evoke a thousand words, a critical spectrum can stimulate a large number of ideas. Figure 10 is one such spectrum. This observation (using the side 1 echelle) has excellent spectral resolution and signal-to-noise.

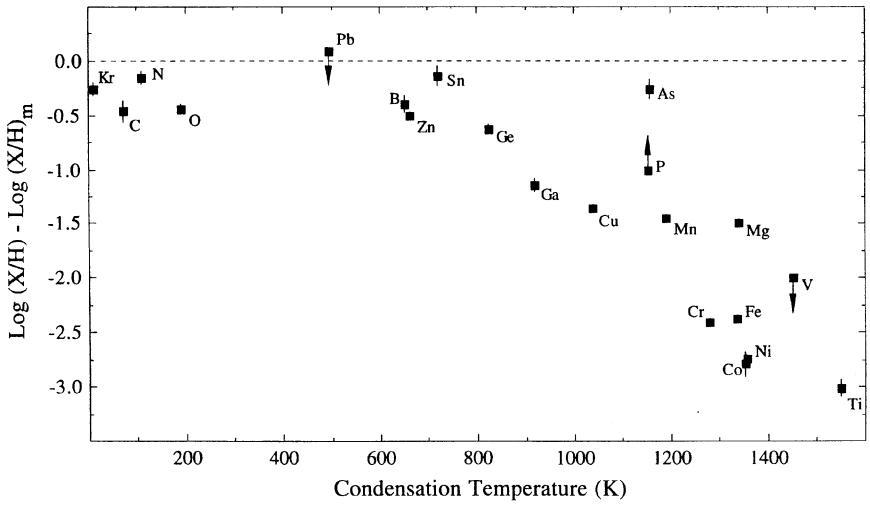

FIG. 9—A plot of the measured abundances, normalized to the meteoritic abundances of Anders and Grevesse (1989), for 21 elements observed with the GHRS in the sight line toward ζ Oph. The data were taken from Cardelli, Savage, and Ebbets (1991), Savage, Cardelli, and Sofia (1992), and Cardelli et al. (1993b) except for B and Co, which were taken from Federman et al. (1993) and As, Sn, and Pb, which were taken from Cardelli et al. (1993c).

The spectrum shows the broad hydrogen Lyman-α emission line formed in the chromosphere of the nearby star Capella and superimposed Lyman-α absorption by interstellar hydrogen and deuterium along the 12.5-pc line of sight towards this star. A nearby star was selected for this observation to avoid the D Lyman-α absorption line being completely swamped by the H Lyman-α absorption. Detailed analysis of this spectrum by Linsky (1992) and Linsky et al. (1993) has determined that the deuterium/hydrogen number density ratio for local interstellar gas is

$$\mathrm{D/H} = 1.65(+0.07, -0.18) \times 10^{-5}.$$

Of course, this value awaits confirmation by observations now planned of other nearby stars, but it looks definitive.

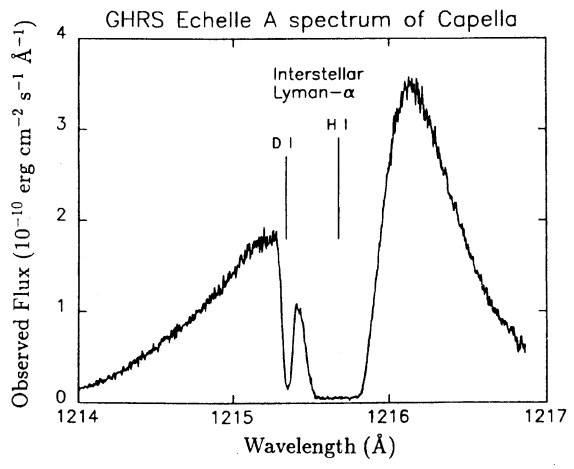

FIG. 10—High-resolution ($\lambda/\delta\lambda = 84{,}000$) spectrum of the Lyman-$\alpha$ region in Capella, showing the interstellar H I absorption and the interstellar D I absorption 0.33 Å away. Residual scattered light in the core of the H I line has not been removed in this presentation.

While the value of D/H is close to the average of many previous determinations, the absolute error in the ratio is far smaller.

All of the deuterium observed today was created between 100 and 1000 s after the onset of the Big Bang. Since then, deuterium has been converted to helium and other elements by nuclear reactions in the centers of stars. As shown in Fig. 11, its abundance relative to hydrogen is a sensitive indicator of the current density of ordinary baryons. This conclusion follows from the relative abundances of the light elements created in the Big Bang being sensitive to the baryon density at that time, and the baryon density today being determined by the density then and the Hubble expansion. The measured abundance ratio of D/H for local interstellar gas along the line of sight to Capella is shown by the thin horizontal line in Fig. 11. The shaded region lying a factor of 1.5–3.0 above this line indicates the likely range of primordial D/H on the basis of chemical evolution calculations for our Galaxy (Steigman and Tosi, 1992) that account for the deuterium lost by nuclear processes in stellar interiors and the return of this deuterium poor material to the interstellar medium by supernovae explosions and stellar winds. The vertical lines indicate the permitted range in today's baryon density in units of the closure or "critical density" necessary to eventually halt the expansion of the universe. It is clear that the density of baryonic matter as estimated from the D/H ratio fails to halt the expansion of the universe by a factor of 10–30. This factor depends somewhat on the assumed value for the Hubble constant, which in Fig. 11 was assumed to be 50 km s^{-1} Mpc^{-1}.

This leaves us with two general scenarios. First, the universe as we know it today had a beginning, but has no end. This may be correct, but many people are uncomfortable with this conclusion as a matter of philosophy and on the basis of observations of the motions of galaxies. Second, the universe may be closed, but here is what that would imply.

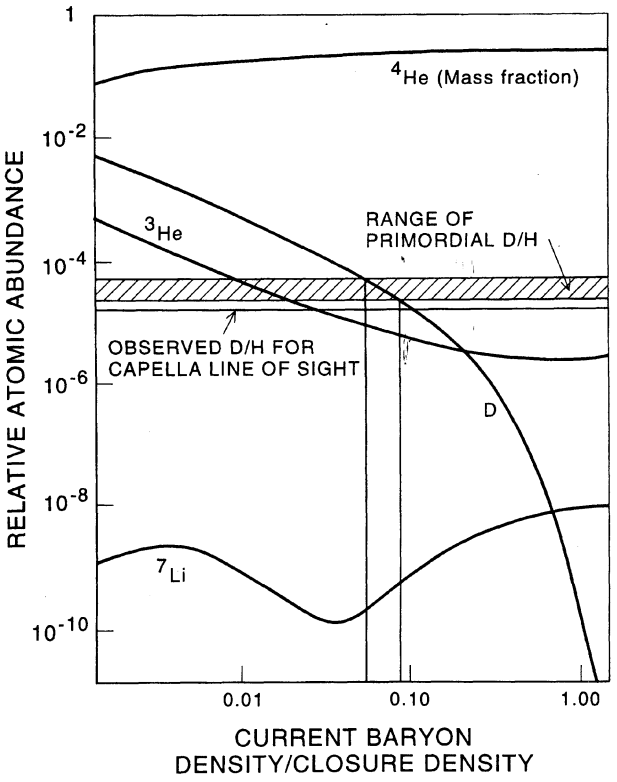

FIG. 11—Implications of the D/H measurement on the baryon density in the universe, assuming standard Big Bang cosmology (e.g., Walker et al. 1991). The baryon density determined by these measurements cannot, by itself, close the universe—see text for discussion.

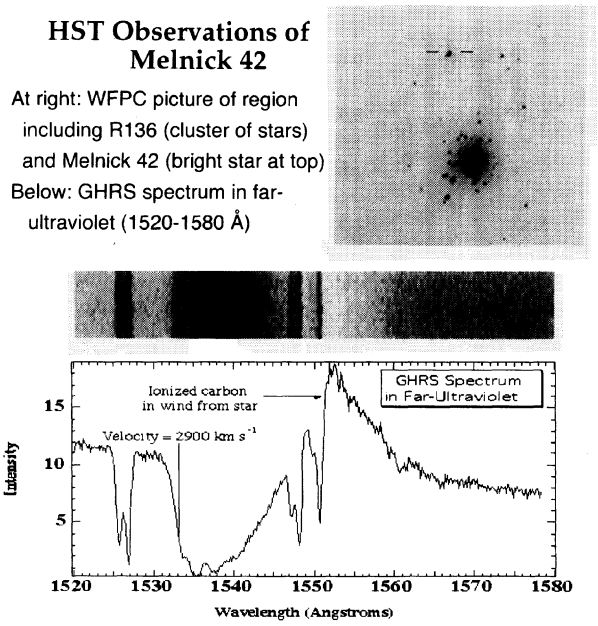

FIG. 12—Presentation of the GHRS spectrum of Melnick 42; see text for discussion.

The composition of the universe would need to be about 2%–10% baryonic (ordinary) matter, depending on the assumed value of the Hubble constant, and the rest in some form of exotic matter not presently detected in any nuclear physics experiment. Proposed choices for the exotic matter include heavy neutrinos, axions (an asymmetry between matter and antimatter), and WIMPS (weakly interacting massive particles). Elementary particle physicists are actively searching for such exotic forms of matter. They are encouraged by studies of galactic rotation curves and the dynamics of clusters of galaxies that indicate that most matter in the universe is dark; that is, the matter does not emit radiation at any wavelength (Tremaine 1992).

If the measurement of D/H in local interstellar gas stands the test of time, it is important because it points to new views of the universe and its composition. It also shows the cosmological implications of a very local measurement.

3.2 Mass Loss by Stellar Winds and the Evolution of the Outer Atmospheres of Stars

3.2.1 Melnick 42 in the Large Magellanic Cloud

Figure 12 shows the spectrum of Melnick 42, an O3f star in the 30 Doradus complex in the Large Magellanic Cloud. The combination of ground-based and UV spectral energy distributions led to the determination of the luminosity, temperature, and radius of the star. It is one of the most luminous and most massive stars known, at $2.5\times10^6\ L_\odot$, with a mass of about 100 $M_\odot$ (Heap et al. 1991). The N V, C IV, and N IV lines show broad P Cygni profiles characteristic of stellar winds. The UV spectrum was analyzed in two ways: by fitting the profiles of the wind lines, assuming an abundance and ionization fraction (Lamers, Cerruti-Sola, and Perinotto 1987), and by a complete synthesis of the wind spectrum with abundances as parameters (Pauldrach et al. 1990). These results are consistent with a slight overabundance in N, and an underabundance of 10–20 times in C. The wind terminal velocity is nearly 3000 km s^{-1} and the mass-loss rate is $\approx4\times10^{-6}\ M_\odot$ yr^{-1}. The model fitting illustrates the

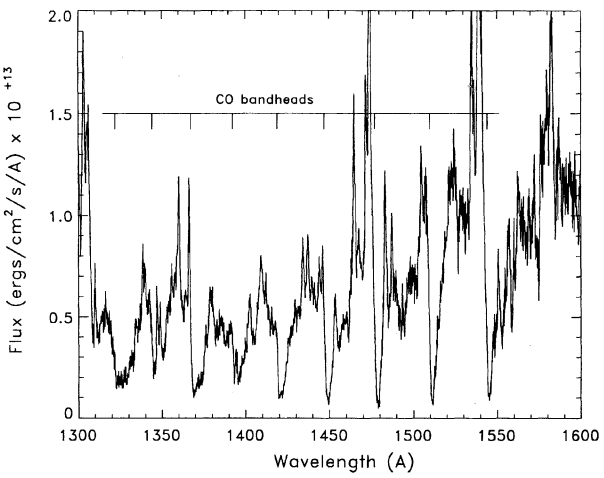

FIG. 13—Spectrum of α Ori showing circumstellar CO absorption features. See text for discussion of implications for weak features seen in IUE data.

complex interplay between metal abundance and stellar wind which is an active area of continued work in the Magellanic Clouds and in other local group galaxies. It also provides an excellent independent consistency check on the stellar radius, mass, and distance (Kudritzki and Hummer, 1990) derived from this analysis and other types of data.

3.2.2 The Outer Atmosphere of α Ori

The prototypical M-supergiant Alpha Orionis is the focus of programs which are designed to probe the chromosphere and circumstellar shell. The goal of these programs is to understand the thermodynamic conditions of these regions and to derive empirical constraints for theoretical modeling of these layers and the stellar wind which joins them. Significant results from the early stages of these programs include the unambiguous detection of a far-UV continuum originating in the chromospheric layers of the star and of superposed absorption bands of the 4th-positive A-X system of CO, which likely originate in the circumstellar shell. These detections provide new diagnostics for the physical conditions in these outer atmospheric regions. Figure 13 shows the portion of a G140L GHRS spectrum containing the circumstellar absorption features.

These data also illuminate the value of the *IUE* archives, in that they allow an objective evaluation of features seen with low signal and low resolution by *IUE*. In this case, it is clear that the features can be seen in *IUE* spectra of α Ori, once you know that they are there. However, it would have been difficult for anyone to have claimed conclusively on the basis of the *IUE* data alone that either the "continuum" or broad absorption features were real and of stellar origin (due to the lower signal/noise of the *IUE* spectrograph, lower resolution, and to concerns regarding the scattering of longer wavelength light, to be picked up by the nonsolar blind *IUE* detectors).

Numerous chromospheric emission features are seen clearly for the first time in the GHRS data, including many additional fluorescent lines of Fe II, pumped by H-Lyman-α. Atomic absorption features due to C I and Fe II are seen in a G160M spectrum centered near 1655 Å. The latter lines are formed at chromospheric temperatures and are clearly not photospheric or circumstellar in origin. (Additional details are provided in Carpenter et al. 1994.)

3.2.3 The Chromosphere of α Tau

The GHRS enables, through its higher resolution, signal to noise, and more precise wavelength calibrations, the direct measurement of flow and turbulent velocities of the magnitude expected in the chromospheres of cool stars. This capability was first demonstrated in the Science Assessment Observations of the K5 red giant Alpha Tauri. G270M and Ech-B spectra, obtained through the SSA, show resolved C II (UV 0.01) intercombination lines near 2325 Å. The position and profiles of these lines indicate a complex turbulent velocity field with a mean value of around 24 km s^{-1} and a mean downflow velocity of the C II plasma of about 4 km s^{-1}. These data indicate complicated small-scale dynamics and provide a rich source of empirical constraints for theoretical modeling of chromospheric heating, such as that undertaken by Judge and Cuntz (1993).

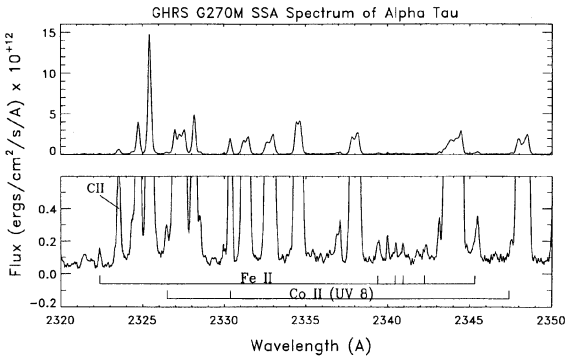

FIG. 14—A 30 Å segment of the spectrum of α Tau showing the dynamic range of the GHRS and some of the Co II and Fe II features described in the text.

The G270M (medium-resolution) spectra also revealed 25 new emission lines in the 2320–2370 Å region, including four lines from Co II (UV 8) and one from Fe I (UV 12). The detection of the Co II lines provide confirmation of the identification, proposed by Carpenter, Wing, and Stencel (1982), of the 2330-Å line as a fluorescent Co II line pumped by a nearby blend of Fe II+Si II at 2344 Å. The Fe I line is a previously unseen product of the well-known Mg II K-Fe I pumping which produces the Fe I (UV 44) lines above 2800 Å.

The large dynamic range and sensitivity of the GHRS is illustrated in Fig. 14, which shows on two different flux scales a 30-Å portion of the 20-min G270M SSA spectrum (smoothed over three data points) of α Tau. The identification of some of the newly detected features, as well as the position of the fluorescent Co II 2330 Å line, are indicated. Further details on the α Tau results can be found in Carpenter et al. (1991).

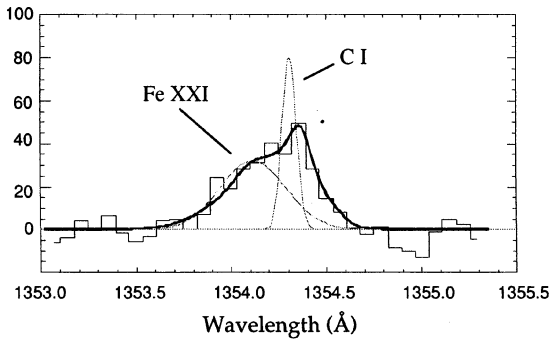

FIG. 15—The observed profiles (histogram) of the overlapping Fe XXI and C I lines near 1354 Å in the spectrum of AU Mic. The dotted curves represent intrinsic Gaussian profiles that, when convolved with the instrumental function, produce the model spectrum (solid curve) that is seen to agree well with the observed data. Details of the modeling procedure are presented by Maran et al. (1994).

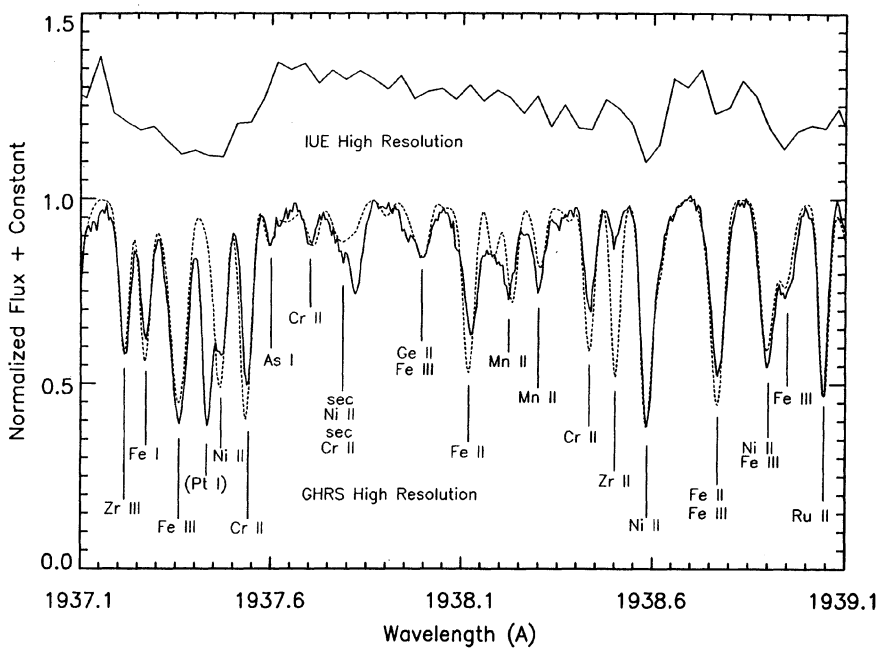

FIG. 16—IUE high dispersion (top), GHRS echelle (bottom, solid), and theoretical (dashed) spectra of χ Lup. Note particularly (from left to right) lines of Zr III, As I, Ge II, Zr II, and Ru II. The lines marked "sec" are from a companion or secondary star.

3.2.4 High Temperature Lines in a Quiescent Red Dwarf

The GHRS has accomplished one of its originally proposed objectives through the first certain detection of the 1354-Å line of Fe XXI on a star, AU Microscopii, other than the Sun (Maran et al. 1991, 1994). This coronal line is formed predominantly at 10 million K. The GHRS medium-resolution spectrum (Fig. 15), obtained on 1991 September 4 at a time when no stellar flare was observed (although the data, in fact, resemble the spectrum of a solar flare), resolved the line, allowing constraints to be placed on bulk motion and turbulent velocity. A cooler coronal line, 1349-Å Fe XII, formed at 1.3 million K, was not evident. However, chromospheric lines of C I, O I, and Cl I were readily seen in the GHRS spectrum extending from 1345 to 1375 Å. This spectrum did reveal emission in the transition region line of O V at 1371 Å, which is formed at 250,000 K. Models of coronal loops in hydrostatic equilibrium are consistent with the observed volume emission measured for Fe XXI and with the upper limit on Fe XII. According to this analysis, the fraction of the photosphere that is covered by the footprints of the coronal loops is less than 14%, if the loop lengths are shorter than the stellar radius.

3.3 Abundances in the Elements and Stellar Evolution—Chi Lup

Approximately 10%–20% of late B- and early A-type stars exhibit an amazing variety of spectral anomalies, of a magnitude and kind not seen elsewhere in the H-R diagram. These are often associated with the presence of surface magnetic fields, or with intrinsically slow rotation, either of which may have the effect of stabilizing mass motions within the photospheric or subphotospheric layers. This naturally leads to theoretical constructs based on the mechanism of radiatively driven diffusion, in which elements, their isotopes, and their various ionization states can become segregated according to their mass and cross sections for the absorption of photons in the wavelength regions of peak radiative flux (e.g., in the ultraviolet for early-type stars). Such models have been extensively developed by Michaud (1970, 1981, 1986) and his collaborators, and have successfully replicated phenomena observed in the chemically peculiar (CP) stars. A notable example is the variation of Mn abundance enhancement as a function of effective temperature observed in the HgMn stars (Smith and Dworetski 1993).

On the other hand, examples can be cited where published predictions of diffusion models do not fully correspond to the observations, for example, the large overabundances of boron observed in 30%–40% of HgMn stars (Leckrone 1981; Sadakane, Jugaku, and Takada-Hida; 1985), while diffusion models predict the complete absence of boron from the photospheres of these stars. We do not understand the heterogeneity of observed abundance anomalies among CP stars of the same generic type. There are surprisingly few well-defined correlations of abnormal abundances with stellar parameters, and so far, the "parameter-free" diffusion models have had only mixed success in explaining those that are observed. It is fair to say that the CP stars remain enigmatic nearly a century after they were first discovered.

Studies of the CP stars from mountain-top observatories are considerably hampered by the paucity of lines in the visible-wavelength spectra of late B and early A dwarfs. Our knowledge of the phenomenology of these stars has been

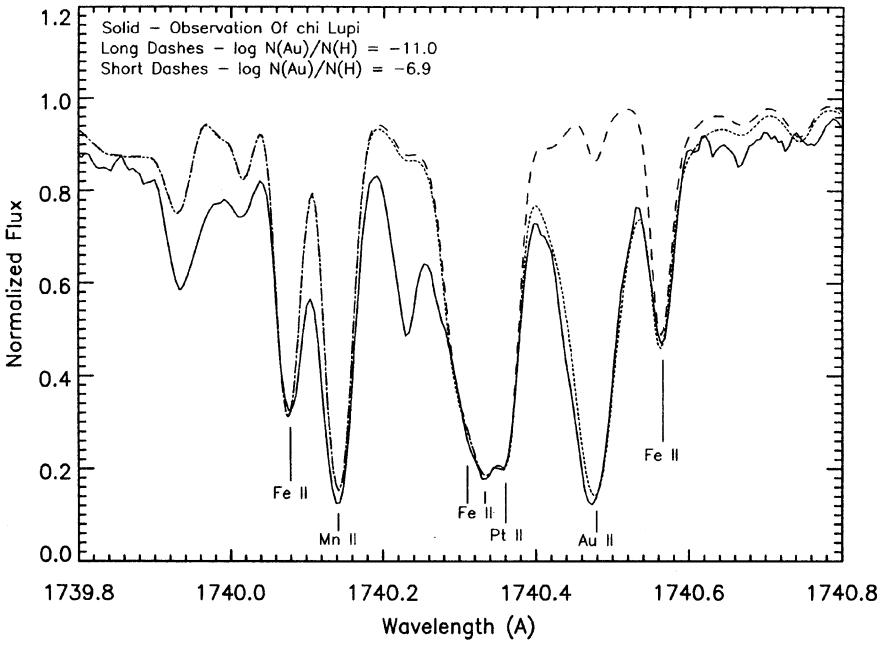

FIG. 17—Observed and calculated spectra of χ Lup, showing the *raie ultime* line of Au II, 1740.475 Å. Long dashes denote calculation for solar gold abundance.

based largely on selection effects resulting from the placement of intrinsically strong lines of particular chemical elements at wavelengths observable from the ground. The enormous enhancement of Hg in the HgMn stars, for example, historically came to light because of the enhanced strength of a single line, Hg II at about 3984 Å (Bidelman 1962). Moreover, it is rare to encounter lines from more than one ionization state of a particular element at visible wavelengths in this effective temperature range. Departures from LTE in the ionization equilibrium may lead to large systematic errors in abundances derived particularly from minority ionization states. These problems are substantially ameliorated by observations at ultraviolet wavelengths, where intrinsically strong resonance and low-excitation transitions of many elements and ionization states occur.

Because of its high resolution, low noise, and linear photometric response, the GHRS is very well suited to precise quantitative spectroscopy of the complex UV spectra of CP stars, many of which are exceedingly sharp lined. To constrain physical models for the origin of abundance anomalies, and perhaps to use the anomalies as probes of the hydrodynamics of photospheric and subphotospheric layers, requires a multidimensional observational approach. One may assess how the abundance of a particular element varies from star to star, as a function of effective temperature, surface gravity, rotational velocity, age, etc. One must also determine how abundances vary from element to element across the periodic table for individual stars. By combining GHRS data with high S/N spectra obtained from the ground, we can for the first time make substantial progress in the latter type of investigation. We have begun a program to obtain pathfinder GHRS echelle observations of selected UV spectral intervals for a small group of sharp-lined, nonmagnetic HgMn CP stars, with the objective of the most comprehensive possible coverage of the periodic table. To date, observations have been acquired in 22 spectral intervals for the cool HgMn star, χ Lup, and in five intervals for the hot HgMn star, Kappa Cancri.

The first observations of χ Lup were centered on the resonance line of Hg II at 1942.3 Å. The spectral resolution of Ech-B at this grating position is approximately 87,000, and was fully realized, despite the *HST*'s spherical aberration, by use of the GHRS SSA. The S/N ratio of the data was about 100 in the continuum. We believe these observations constitute the most detailed ultraviolet spectrum of a star other than the sun ever obtained. A sample of this observation, together with the best current spectrum synthesis calculation, is illustrated in Fig. 16.

Subsequent analyses of this observation (Leckrone, Wahlgren, and Johansson 1991) confirmed the mercury abundance and isotope anomalies first noted in the 3984-Å Hg II line. The observed Hg II line profile is consistent with an isotope mixture comprising 99% ^{204}Hg, the heaviest stable Hg isotope. The total Hg abundance is approximately five orders of magnitude larger than found in solar system material. Further early analysis of the data (Leckrone et al. 1993a) has yielded overabundances of other heavy elements, such as Ge, As, Zr, and Ru, and underabundances of Co, Ni, Cu, and Zn in χ Lup. We have measured extreme abundances of Pt and Au, rivaling in magnitude the overabundance of Hg (Wahlgren et al. 1993), as illustrated in Fig. 17. The triad Pt-Au-Hg appears to stand out as an abundance peak in Fig. 18. A search for UV lines of the contiguous elements in the periodic table, Os, Ir, Tl, Pb, etc., is currently underway.

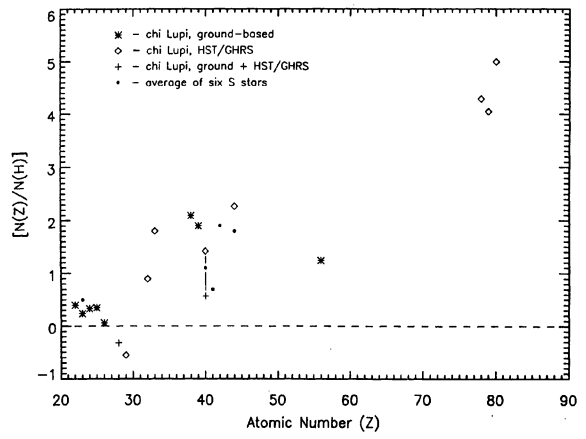

FIG. 18—Abundances of heavy elements relative to solar values (in logarithmic units) derived to date for χ Lup. For comparison, published abundances for six cool S-type (heavy metal) stars are also shown (Wallerstein 1984).

Further evidence of the importance of coordinated UV and optical-wavelength observations is the discordance between abundances we have determined for different ionization stages of Zr. The abundance derived from both optical and UV lines of Zr II is nearly a full order of magnitude lower than that for Zr III, as determined from our GHRS data. We cannot yet say whether this discordance is due to a non-LTE ionization balance, or to diffusive segregation of the Zr ions within the outer layers of χ Lup.

The GHRS observations of χ Lup have also stimulated research in atomic spectroscopy. At this unprecedented UV spectral resolution, absorption features previously observed to be hopelessly blended at *IUE* high dispersion ($\lambda/\delta\lambda = 12{,}000$) are now seen to separate beautifully into their constituent components (Fig. 16). Our initial synthetic spectrum calculations highlighted the inadequacies in the current state of atomic data—oscillator strengths, wavelengths, nuclear effects—needed to fit the observed spectral line positions and strengths (Leckrone et al. 1993b). For example, the estimated relative wavelength accuracy of the GHRS echelle mode is 2 mÅ. Absolute accuracies at this same level can be achieved by tying line positions for Mn, Fe, Ni, etc., observed in the stellar spectrum to laboratory Fourier transform spectrometer (FTS) measurements for the same transitions, which are accurate to about ± 0.1 mÅ. In contrast, published wavelengths for UV transitions, based in some cases on decades-old laboratory measurements, are often uncertain by ± 10–20 mÅ or more. While the GHRS data pose a challenge to atomic spectroscopy, they synergistically provide new information regarding atomic structure. Wavelengths and relative line strengths measured with the GHRS for transitions that are difficult to observe under laboratory conditions will lead to more accurate energy levels and atomic structure models for the lower ionization stages of many elements, and to improved knowledge of configuration interactions and level mixing.

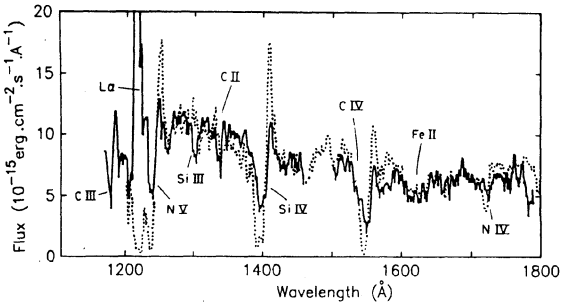

FIG. 19—Spectrum (smoothed over 3 Å) of starburst knot No. 2 in NGC 1068. The P Cyg profiles of N V, Si IV, and C IV, and the geocoronal Lyman-α, are clearly visible. The dotted line represents an IUE spectrum (redshifted and unreddened) of the O7Iaf star, HD 163758.

3.4 Extragalactic Sources

3.4.1 NGC 1068

Figure 19 shows the spectrum of starburst knot No. 2 in the galaxy NGC 1068 (Hutchings et al. 1991). Lying in the circumnuclear region of this Seyfert Galaxy, its stellar population can tell us something of the recent history of this active galaxy. The spectrum is dominated by hot, young, massive stars characterized by the strong UV continuum and the strong P Cyg line profiles of N V, Si IV, and C IV. Note that the high sensitivity of the GHRS is essential for the resolution and signal-to-noise necessary for this work.

The spectrum can be reproduced by a mix of hot stars defined by an initial mass function (IMF). It can also be fit with a synthesis of *IUE* spectra ranging from O7 to B2. However, the ground-based flux from the knot indicates that there are few lower-mass stars. The results indicate that the starburst knot contains several thousand O and B stars which formed in a single episode about 3 million years ago. The whole complex has about the same luminosity as the 30 Doradus nebula in the LMC.

The terminal velocity from the stellar wind lines is about 1900 km s^{-1}, which suggests that the abundances are similar to our Galaxy.

3.4.2 Lyman-α forest in 3C 273

Absorption lines due to Lyman-α ("the Lyman-α forest lines") are produced by clouds of hydrogen along the line of sight between our galaxy and distant quasars (Lynds 1971). Since the Lyman-α line has a wavelength of 1216 Å, these lines can only be observed from ground-based telescopes for cloud distances sufficiently large that the cosmological redshift places their absorption at observed wavelengths greater than about 3200 Å. Until the launching of the *HST*, nothing was known about the nearby Lyman-α clouds (Bergeron, Savage, and Green 1987). Because of light travel times, this is equivalent to saying that we knew something about these clouds early in the evolution of the universe, but nothing about them at the present epoch. The observations from the ground showed that the number of Lyman-α lines was rap-

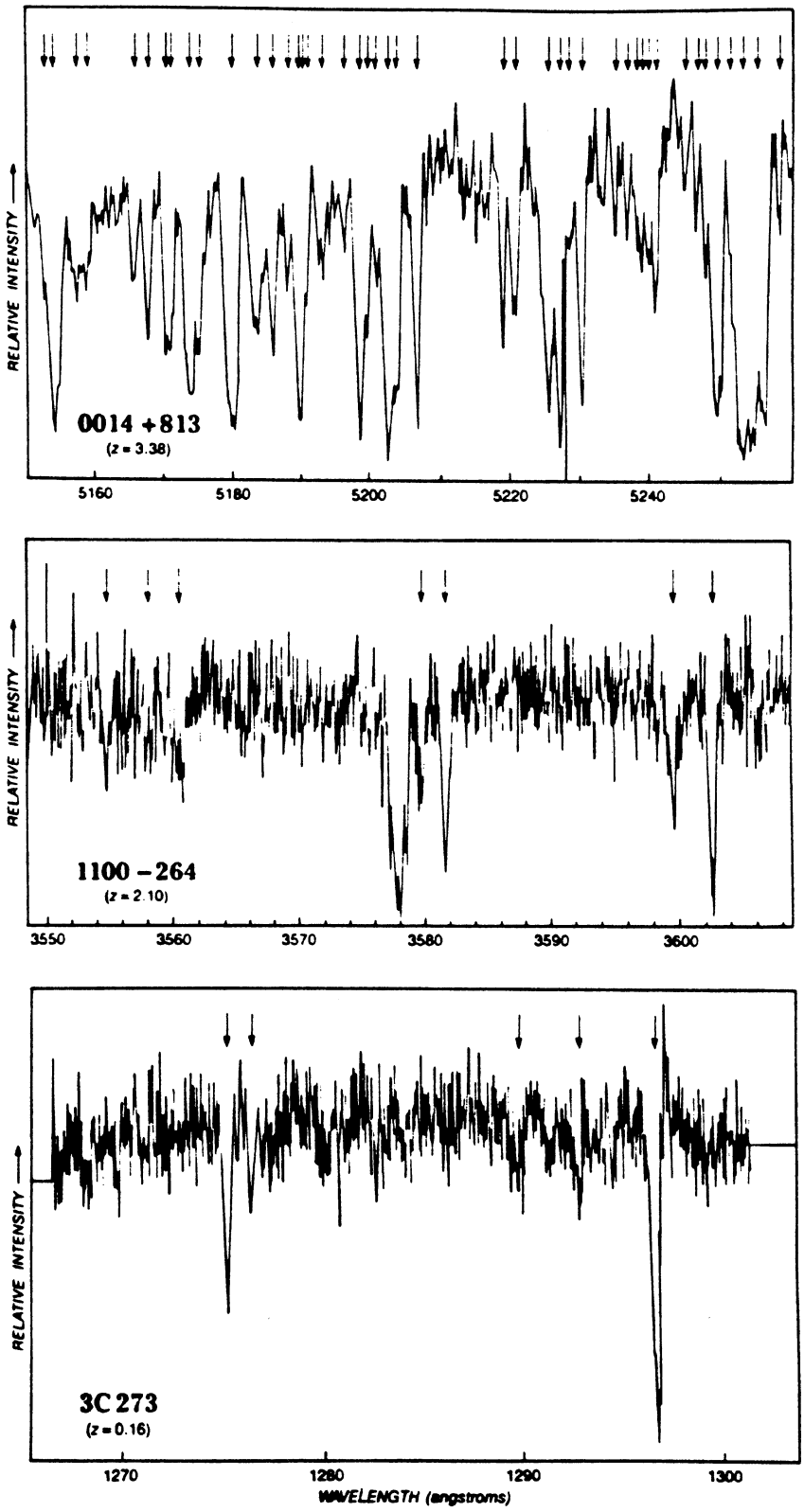

FIG. 20—Spectra of quasars with z values of 3.38, 2.10, and 0.16. The top two are ground-based observations and the bottom one is from the GHRS. The arrows mark Lyman-α forest absorption features.

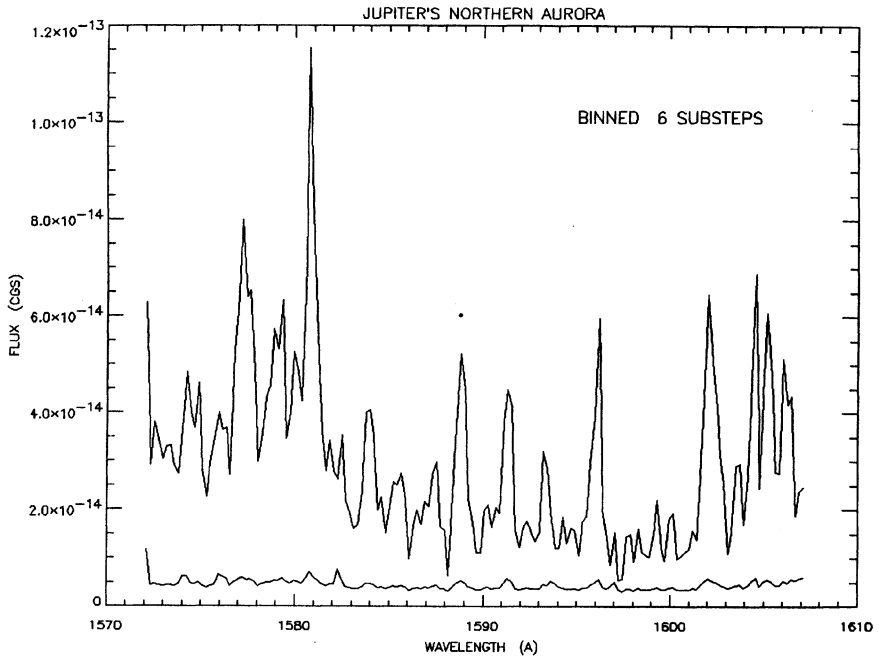

FIG. 21—Jupiter's northern aurora in the Lyman band of H_2 binned over three-diode channels (effective resolution 0.24 Å). The location is at System III longitude 180 deg and latitude +65 deg which misses the region of brightest emission. The propagated error vector is shown below. The flux is overestimated because it assumes the aperture transmission for a point source rather than for an extended emission area.

idly decreasing with decreasing redshift, and if this trend had continued to the present, at zero redshift there would have been virtually no Lyman-α lines to study.

The GHRS observed the Lyman-α forest along the line of sight to the nearby bright quasar 3C273, and these observations showed, somewhat unexpectedly, that the rapid decrease indicated at high redshift does not extend to zero redshift. Figure 20 shows quasar spectra for three values of the redshift: 3.4, 2.1, and 0.2. The Lyman-α lines for each spectrum are marked by the arrows at the top. The top and middle spectra are from ground-based observations and the bottom spectrum is from the GHRS. The other absorption lines in the 3C273 spectrum are caused by interstellar gas in our galaxy. The change in the number of Lyman-α lines between redshifts of 2.1 and 0.2 is consistent with a population of Lyman-α clouds which are neither created nor destroyed and whose sizes have not significantly changed over this interval (Morris et al., 1991; also see Brandt et al. 1993).

One of the more interesting questions about the Lyman-α clouds is their relation to galaxies: Are the clouds orbiting in or near ordinary galaxies, are they held together by the gravitational force of "dark matter," themselves thus constituting small "unborn" galaxies, or, as initially proposed, are they confined by very hot intergalactic gas with no relation to ordinary galaxies? Preliminary follow-up observations of the galaxies near the line of sight to 3C273 by Morris et al. (1993) show that some of these low redshift Lyman-α clouds are not intimately associated with ordinary galaxies, but neither are the clouds randomly distributed. Instead, they show a statistically significant tendency to mildly cluster with galaxies.

To pursue this question further, the restoration of the G140L grating of side 1 is of vital importance for it provides by far the best combination of sensitivity, spectral coverage, and resolution to allow many more low redshift lines of sight to be studied. While the luxuriant growth of the very high redshift Lyman-α forest has given way to a rather arid savannah at low redshifts, their continued study is proving of importance for addressing the fundamental question of the origin and evolution of galaxies and clusters of galaxies.

3.5 The Solar System—The Jovian Aurora

The first observations of Jupiter's aurora were made as part of a *HST* campaign to monitor Jupiter's FUV emissions during the flyby of the *Ulysses* spacecraft from 1992 February 6 to 9. The objective was to obtain near-simultaneous data of the time-variable aurora which referred to the same auroral state. FOC images in three wavelength bands covering H Lyman-α and the Werner and Lyman bands of H_2 were obtained. The GHRS was used with the medium-resolution grating G160M and the LSA to observe 35-Å intervals centered near the peaks of the Werner and Lyman H_2 bands; i.e., 1270 and 1590 Å. These observations were made on 8 February from 17:10 to 19:30 UT. Blind pointing was used to observe the region of expected maximum intensity based on the large-aperture *IUE* observations, longitude 180° and latitude +65°, and this region was tracked as Jupiter rotated.

Figure 21 shows the emission from the Lyman bands and

continuum of molecular hydrogen for Jupiter's northern aurora. Essentially all of the observed emissions are due to H_2. The individual vibration-rotation bands are visible even though the spectrum has been binned over channels three-diodes (six substeps) wide to improve the signal-to-noise ratio. This was necessary because the region of maximum emission was missed owing to an unexpected longitudinal distribution of the H_2 emission. The FOC images showed that the auroral emission was not maximum at 180° longitude; it was closer to a minimum. The *IUE* result was an artifact of its large aperture, which heavily weighted the projected area of the entire auroral zone, which was maximum at this longitude. In spite of this, however, H_2 auroral emission is clearly detected with the GHRS. In contrast to the FOC, whose filters have red leaks, the solar blind GHRS reveals very little scattered light from longer wavelengths; comparison spectra taken at low Jovian latitudes were essentially dark.

Analysis reveals a rotational-vibration temperature for the H_2 in this region of the aurora of 550 K (Trafton, Gerard, and Waite 1994). This is below the 850–1100 K measured for H_3^+ in the near infrared (Drossart et al. 1989; Maillard et al. 1990; Miller and Tennyson 1990). This is probably indicative of the different auroral region observed by the GHRS and the different effective altitudes for formation of the H_2 and H_3^+ emissions.

4. SUMMARY AND THE FUTURE

The GHRS has been producing its spectra on a routine basis and delivers the promise of *HST* in terms of high spectral resolution results. The repairs to the *HST* and the GHRS during the first servicing mission have been tested as part of the verification activities. Specifically, the GHRS now receives greatly improved images from COSTAR, and side 1 (Ech-A and G140L) is available for use. To increase the scientific productivity of the GHRS after the successful first servicing mission, we need significantly improved operational efficiency, and moving-target tracking capability.

The GHRS is now a fully operational instrument on *HST* and we are optimistic that the GHRS will continue to carry out a full and efficient suite of observations.

The GHRS is a team effort requiring input from scientists, engineers, technicians, computer specialists, managers, administrative personnel, etc. The scientists who make up the GHRS Investigation Definition Team (IDT) are the first 16 authors of this paper. The GHRS Team has functioned very well for a long time, and the IDT wishes to thank all for their contribution to the success of the GHRS. We thank Carolyn Collins Petersen for expert editorial assistance in preparing this paper. We also acknowledge the support from NASA via numerous contracts and grants which have funded the development of the GHRS, and operations and data analysis support for the GHRS team.

REFERENCES

Anders, E., and Grevesse, N. 1989, Geochim. Cosmochim. Acta, 53, 197
Baity, W. A., et al. 1993, SPIE Orlando/93, 1945
Beaver, E. A., et al. 1992, Photoelectronic Image Devices, ed. B. L. Morgan (England, IOP)
Bergeron, J., Savage, B. D., and Green, R. F., 1982, in Exploring the Universe with the IUE Satellite, ed. Y. Kondo et al. (Dordrecht, Reidel), p. 803
Bidelman, W., 1962, Sky and Telescope, 23, 140
Brandt, J. C., et al. 1993, AJ, 105, 831
Brandt, J. C., 1991, in The First Year of HST Observations, ed. A. L. Kinney and J. C. Blades (Baltimore, STScI), p. 106
Brandt, J. C., et al. 1979, Proc. SPIE, 172, 254
Brandt, J. C., et al. 1981, Proc. SPIE, 279, 183
Brandt, J. C., et al. 1982, IAU Spec. Sess. Comm., 44, 76
Brandt, J. C., et al. 1984, Proc. SPIE, 445, 427
Cardelli, J. A., et al. 1989, ApJ, 365, 789
Cardelli, J. A., et al. 1991a, ApJ, 377, L57
Cardelli, J. A., Savage, B. D., and Ebbets, D. C., 1991b, ApJ, 383, L23
Cardelli, J. A., et al. 1993a, ApJ, 413, 401
Cardelli, J. A., Mathis, J. S., Ebbets, D. C., and Savage, B. D. 1993b, ApJ, 402, L17
Cardelli, J. A., Federman, S. R., Lambert, D. L., and Theodosiou, C. E. 1993c, ApJ, 416, L41
Carpenter, K. G., et al. 1994, ApJ, 428, 329
Carpenter, K. G., et al. 1991, ApJ, 377, L45
Carpenter, K. G., Wing, R. F., and Stencel, R. E. 1982, BAAS, 14, 614
Drossart, P., et al. 1989, Nature, 340, 539
Ebbets, D. C. 1992, Final Report of the Science Verification Program for the Goddard High Resolution Spectrograph for the Hubble Space Telescope, Ball Aerospace Systems Group
Ebbets, D. C., Brandt, J. C., and Heap, S. R. 1991, in The First Year of HST Observations, ed. A. L. Kinney and J. C. Blades (Baltimore, STScI), p. 110
Ebbets, D. C., and Garner, H. W. 1986, Proc. SPIE, 627, 638
Ebbets, D. C., and Brandt, J. C. 1983, PASP, 95, 543
Eck, H., Beaver, E., and Shannon, J. 1985, Advances In Electronics and Electron Physics, ed. B. L. Morgan, p. 141
Federman, S. R., Sheffer, Y., Lambert, D. L., and Gilliland, R. I. 1993, ApJ, 413, L51
Heap S. R., et al. 1991, ApJ, 377, L29
Heap, S. R., et al. 1994, submitted to PASP
Hobbs, L. M. 1969, ApJ, 157, 135
Hobbs, L. M., Welty, D. E., Morton, D. C., and Spitzer, L. 1993, ApJ, 411
Hutchings, J. B., et al. 1991, ApJ, 377, L25
Judge, P., and Cuntz, G. 1993, ApJ, 409, 776
Kudritzki, R. P., and Hummer, D. G. 1990, ARAA, 28, 303
Lamers, H. J. G. L. M., Cerruti-Sola, M., and Perinotto, M. 1987, ApJ, 314, 726
Leckrone, D. S. 1981, ApJ, 250, 687
Leckrone, D. S., Wahlgren, G. M., and Johansson, S. G. 1991, ApJ, 377, L37
Leckrone, D. S., et al. 1993a, IAU Colloq. No. 138, ed. M. M. Dworetski, F. Castelli, and R. Faraggiana (San Francisco, ASP), p. 42
Leckrone, D. S., Johansson, S. G., Wahlgren, G. M., and Adelman, S. J. 1993b, Phys. Scripta, T47, 149
Linsky, J. L. 1992, ESO Conference and Workshop Proceedings, No. 44, p. 33
Linsky, J. L., et al. 1993, ApJ, 402, 694
Lynds, C. R. 1971, ApJ, 164, L73
Maillard, J. P., et al. 1990, ApJ, 363, L37
Maran, S. P., et al. 1991, BAAS, 23, 1382

Maran, S. P., et al. 1994, ApJ, 421, 800
Michaud, G. 1970, ApJ, 160, 641
Michaud, G. 1981, in Upper Main Sequence Chemically Peculiar Stars, ed. P. Renson (Liege, University of Liege), p. 355
Michaud, G. 1986, in Upper Main Sequence Stars With Anomalous Abundances, I.A.U. Colloq. No. 90, ed. C. R. Cowley, M. M. Dworetski, and C. Megessier (Dordrecht, Reidel), p. 459
Miller, S., Joseph, R. D., and Tennyson, J. 1990, ApJ, 360, L55
Morris, S. L., et al. 1991, ApJ, 377, L21
Morris, S. L., et al. 1993, ApJ, 419, 524
Pauldrach, A., Kudritzki, R. P., Puls, J., and Butler, K. 1990, A&A, 228, 125
Reader, J., et al. 1990, ApJ Suppl., 72, 831
Rosenblatt, E. I., et al. 1991, Proc. SPIE, 1449, 72
Sadakane, K., Jugaku, J., and Takada-Hidai, M. 1985, ApJ, 297, 240
Savage, B. D., Cardelli, J. A., and Sofia, U. J. 1992, ApJ, 401, 706
Savage, B. D., et al. 1991, ApJ, 377, L53
Sheffer, Y., Lambert, D. L., Federman, S. R., and Cardelli, J. A. 1992, ApJ, 397, 482
Smith, A. M., et al. 1991, ApJ, 377, L61
Smith, K. C., and Dworetski, M. M. 1993, A&A, 274, 335
Steigman, G., and Tosi, M. 1992, ApJ, 401, 150
Trafton, L., Gerard, J. C., Munhoven, G., and Waite, H. 1994, ApJ, 421, 816
Tremaine, S. 1992, Phys. Today, 45, 28
Tripp, T. M., Cardelli, J. A., and Savage, B. D. 1994, AJ, 107, 645
Wahlgren, G. M., et al. 1993, IAU Colloq. No. 138, 121
Walker, T. P., et al. 1991, ApJ, 376, 51
Wallerstein, G. 1984, JOSA B, 1, 307
Wasson, J. T. 1985, Meteorites: Their Record of the Early Solar System History (New York, Freeman), p. 250
Wertz, J. R., ed. 1978, Spacecraft Attitude Determination And Control (Holland, Reidel)